MANUSCRIPT

Modeling crowd pressure and turbulence through a mixed-type continuum approach

Haoyang LIANG[a], Liangze YANG[b], Jie DU[c,d,e], Chi-Wang SHU[f] and S. C. WONG[g]

[a]Key Laboratory of Road and Traffic Engineering, Ministry of Education, Tongji University, Shanghai 201804, China;
[b]School of Mathematical Sciences, Anhui University, Hefei, Anhui 230601, China;
[c]School of Mathematical Sciences, East China Normal University, Shanghai 200241, China
[d]Shanghai Key Laboratory of PMMP, East China Normal University, Shanghai 200241, China
[e]Key Laboratory of MEA, Ministry of Education, China
[f]Division of Applied Mathematics, Brown University, Providence, RI 02912, USA.;
[g]Department of Civil Engineering, The University of Hong Kong, Hong Kong, China

ARTICLE HISTORY
Compiled March 3, 2024

ABSTRACT
Empirical studies of large gatherings and natural disasters have revealed two important features of dense crowds: extremely high crowd pressure and crowd turbulence. In this study, a mixed-type continuum model for multidirectional pedestrian flow was developed that explicitly considered the phase transition of different anticipation characteristics under different densities. Non-hyperbolicity was used to model the strong instabilities during crowd turbulence. In addition, by estimating the aggregated crowd pressure, the proposed model could clarify the effects of both force chains and panic sentiment, phenomena commonly observed during crowd disasters. The non-hyperbolic partial differential equations were solved using the mixed-type finite difference method, and Eikonal equations were solved using the fast sweeping method. Subsequently, the continuum model was applied to simulations of two real-world scenarios – the 2015 Hajj crowd disaster and the 2010 Love Parade crowd disaster – and validated through comparison with empirical observations. Overall, the proposed model is an efficient tool for evaluating crowd management strategies to predict and assess the crowd state.

KEYWORDS
crowd dynamics; phase-transition; continuum modeling; numerical algorithm; crowd turbulence

1. Introduction

Over the past two decades, crowd disasters have caused thousands of deaths worldwide (Still 2022). Such disasters commonly occur during religious gatherings, such as the 2015 Saudi Arabia Hajj Disaster (2,431 deaths), and large-scale events, such as the 2010 Love Parade disaster (652 injuries) and 2022 Seoul Halloween crush (156 deaths). The high fatalities resulting from such disasters are a primary concern for governments and event organizers, and researchers have made significant efforts to design realistic simulations that can be used to strategically prevent such tragedies.

CONTACT S. C. WONG Email: hhecwsc@hku.hk

Figure 1 shows a general framework for describing the mechanism of crowd disasters based on a review of empirical studies of crowd disasters (Helbing and Mukerji 2012; Benedictus 2015; Haghani et al. 2019). The two important features of crowd dynamics that distinguish dangerous situations from normal pedestrian flow are high crowd pressure and crowd turbulence. During crowd disasters, fatalities typically occur due to suffocation, induced by high crowd pressure, and stampedes, which result from turbulence. Crowd pressure and turbulence can be mathematically modeled and must be thoroughly studied. However, it is challenging to describe the aggregating feature of pushing forces, and thus, only a few models can quantitatively reproduce high crowd pressure, which has been estimated to range from $1,000$ N/m to $2,000$ N/m during crowd disasters (Dickie and Wanless 1993; Smith and Lim 1995). Moreover, it is difficult to establish a model that can reflect the stability of pedestrian movement under normal situations and reproduce crowd turbulence in dangerous situations.

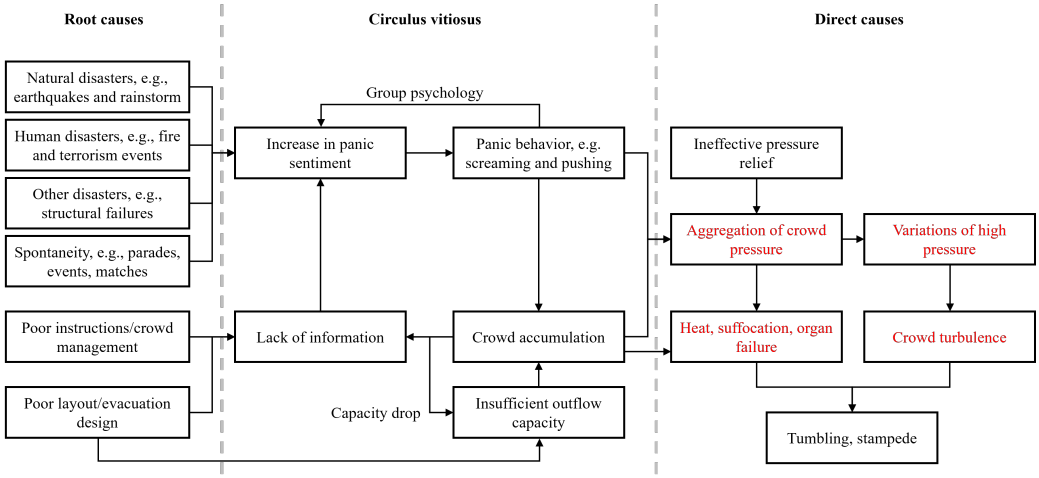

Figure 1.: **The mechanism of crowd disasters involves three stages.** The first stage pertains to the root causes. In the second stage, panic sentiment gradually increases, and a crowd accumulates, forming an amplifying feedback circle. The formation of this circle represents the critical process that may lead to a crowd disaster. The third stage is characterized by falling, trampling, and fatalities owing to direct causes (marked in red). With increasing crowd pressure and limited oxygen, physically vulnerable people are likely to be the first to succumb to coma, suffocation, or organ failure, which are the direct causes of death in most cases.

Recent model-based studies have utilized microscopic models to quantify and characterize crowd dynamics under hazardous scenarios. Traditional agent-based models, social force models, and discrete element models have been developed to approximate actual contact force (Helbing et al. 2000; Langston et al. 2006; Liu et al. 2017). A recent modification of the social force model (Wang et al. 2023) depicted crowd force using particle analogies, with calibration based on experiments and evaluation of danger in previous crowd disasters. However, since microscopic models focus on individual characteristics, they tend to overlook the influence of propagated forces among crowds, consequently underestimating crowd pressure in dense scenarios. As observed in real crowds (Helbing et al. 2007; Helbing and Mukerji 2012), force chains can form due to inadvertent physical interactions between individuals, causing crowd pressure to vary significantly and become almost uncontrollable. This property bears a striking resemblance to fluid pressure and has inspired recent studies to apply hydrodynamics

from a macroscopic perspective to describe the dense movement of crowds.

In macroscopic models, crowd movement is perceived as fluid, taking into account the relationship between microscopic properties such as density, speed, and flow. Hughes (2002) initially proposed a first-order continuum model based on the hydrodynamic properties of moving crowds, factoring in the route strategy. Jiang et al. (2010) and Zhao et al. (2019) further developed high-order continuum models that successfully reproduced complex phenomena such as lane formation and stop-and-go waves. Recently, macroscopic models have been further refined to reproduce the dense, high-pressure crowds that form during crowd disasters, explicitly considering the effect of panic on pedestrian behaviors (Liang et al. 2021). However, existing models have primarily focused on unidirectional crowd dynamics and have not yet taken into account the interactions between multidirectional pedestrian flows under dense scenarios, which are present in most crowd disasters, such as the recent Seoul Halloween crowd crush (F. 2022).

In addition to the inadequate consideration of the influence from collisions of multidirectional pedestrian streams, another significant phenomenon, crowd turbulence, has not been sufficiently addressed in existing models. Based on empirical studies (Johansson et al. 2008; Helbing and Mukerji 2012), crowd turbulence is considered to be associated with shock waves that fluctuate crowd pressure, which can be so powerful that they can even lift people off the ground. The strong instability of crowd movement presents a significant challenge to existing macroscopic models, where the hyperbolic nature of the Euler equations in the current continuum models (Huang et al. 2009; Liang et al. 2021) restricts the solutions to be unique and stable. This limitation raises an important question: Could a non-hyperbolic continuum model be more suitable for describing crowd dynamics during crowd disasters?

The aim of this study was to develop a higher-order continuum model for multidirectional pedestrian flows to simulate crowd pressure and crowd turbulence as observed in crowd disasters. Unlike previous continuum models that adhered to hyperbolic laws, this model introduced novel assumptions about the key parameters, formulating non-hyperbolic Euler equations for the conservation equation set. Details of the problem statement are presented in Section 2. Based on the non-hyperbolic assumption, a continuum model for multidirectional pedestrian flow and its corresponding numerical solution are established in Sections 3 and 4, respectively.

In Section 5, the proposed model was applied to real-world disaster scenarios, and the results were compared with observed data using video analysis technology. In general, when comparing simulation results with empirical data, it is challenging to quantify observed phenomena, such as crowd turbulence. Krausz and Bauckhage (2012) proposed a method to detect crowd dynamics from videos in an automated manner. Khan (2019) described the oscillation map by investigating the individuals stuck in congested areas, which was further applied to the detection of crowd anomalies using pre-trained deep learning models. Similarly, levels of chaotic movement, such as turbulence pressure (Helbing et al. 2007) and velocity entropy (VE) (Wang et al. 2019), have been used as indicators of crowd turbulence. In this study, the particle image velocimetry method (PIV) (Thielicke and Sonntag 2021) was introduced to derive the VE from video recordings. The effectiveness of the multidirectional model was validated through qualitative evaluations of the simulation results and quantitative comparison of the video recordings with the simulation results.

2. Problem statement

Predictive management of heterogeneous crowd movement during large events such as parades, matches, or tourism gatherings is important but challenging. In these situations, pushing and fear can lead to chaos and confusion, making it difficult to predict unstable movement under panic situations. The problem is particularly acute when there are multidirectional pedestrian streams, which aggravate the congestion and increase the collision forces. Addressing these challenges requires a robust model to describe the evolution of crowd states based on explicit mechanisms of crowd pressure and crowd turbulence.

Based on the unidirectional pedestrian model that considered pushing forces and panic effect (Liang et al. 2021), this study further investigates the moving characteristics of multidirectional pedestrian flows through a fundamental diagram under intersecting situations (Wong et al. 2010). More importantly, the anticipation assumption is further developed to capture the "phase transition" of pedestrian movement between different density levels. According to a post-disaster analysis (Helbing et al. 2007), there is a significant transition in the phase of crowd movement from laminar to turbulent flow, exhibiting a clear boundary across the entire region. This phenomenon is captured in the long exposure photographs (see Figure 2a)) and in the figure presented by Johansson et al. (2008). These observations suggest a distinctly different state of crowd behavior characterized by substantial instability, referred to as crowd turbulence. The emergence of this phase transition is a crucial precursor to potential hazards. Once such a transition occurs (see Figure 2b)), a crowd disaster is more likely to happen.

(a) 2010 Love Parade disaster (Loveparade 2011)

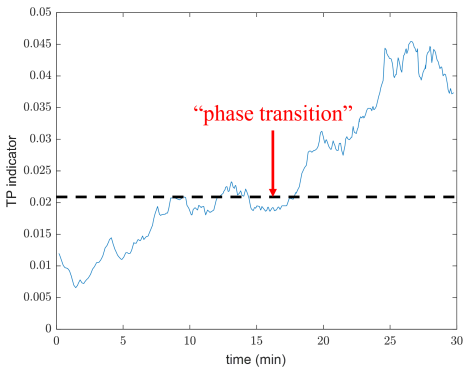

(b) 2006 Hajj disaster (Helbing et al. 2007)

Figure 2.: Observation of "phase transition" during crowd disasters. (a) A long-term photograph between 16:38:10 and 16:38:20 (Loveparade 2011). (b) Evolution of "Turbulence Pressure" (TP) during 2006 Hajj disaster, which is an indicator to quantify crowd turbulence (Helbing et al. 2007).

The widely-used acceleration equation (Equation (1)) incorporates an anticipation pressure to describe the continuum of momentum in crowd dynamics, which depends on the density and is denoted as $P_1 = h(\rho)$ Jiang et al. (2010); Liang et al. (2021); Yang et al. (2023). The assumption of a monotonically increasing relationship between this pressure and density in these studies has revealed two inherent problems. First, from the perspective of physical meaning, individuals are less likely to think independently during crowd turbulence, which questions the existence of the anticipation term under

high-density situations. Second, from the perspective of mathematical formulation, the strong instability questions the applicability of hyperbolic systems after phase transition: If $h'(\rho)$ is nonpositive, the Euler equation set can be parabolic or elliptic, which requests the development of a mixed-type solution algorithm. To address these problems, the main aim of this study is to develop a mixed-type model and corresponding numerical algorithms to capture the phase-transition characteristic in crowd disasters.

$$\partial_t \mathbf{V} + (\mathbf{V} \cdot \nabla)\mathbf{V} + \frac{h'(\rho)}{\rho}\nabla\rho = \text{RHS}, \tag{1}$$

where $\frac{h'(\rho)}{\rho}\nabla\rho$ describes the anticipation effect.

3. Model description

This section describes the assumptions incorporated into the novel continuum model framework for multidirectional pedestrian flow to reproduce the complex crowd phenomena in real crowd disasters, i.e., crowd pressure and turbulence. Please refer to Appendix C for the definitions of symbols and functions used in this study.

3.1. *Assumptions*

Assumption 1. *The pedestrians are divided into K groups with characteristic crowd dynamics that follow the continuity of mass and momentum.*

The local density of the k-th pedestrian group, $\rho^{(k)}$ is defined as the number of pedestrians within a unit area. $\mathbf{V}_e^{(k)} = (u_e^{(k)}, v_e^{(k)})$ is the expected speed vector, i.e. the equilibrium pedestrian velocity when the effect of physical contact is not considered, with u_e and v_e denoting the velocities in the x and y directions, respectively. $\mathbf{V}^{(k)} = (u^{(k)}, v^{(k)})$ is the actual speed vector, defined as the actual average pedestrian velocity, with u and v representing the velocities in the x and y directions, respectively. The movement of each pedestrian group follows fluid dynamics concepts, and the set of continuity equations is applied. For convenience, the following notation is defined: $[e_1, e_2, ...]^{(k)} = [e_1^{(k)}, e_2^{(k)}, ...]$.

$$\mathbf{Q}_t^{(k)} + \mathbf{F}_x^{(k)} + \mathbf{G}_y^{(k)} = \mathbf{S}^{(k)}/\bar{m}, \tag{2}$$

where $\mathbf{Q}_t^{(k)} = \partial([\rho; \rho u; \rho v]^{(k)})/\partial t$ is the change in mass and momentum; $\mathbf{F}_x^{(k)} = \partial([\rho u; \rho u^2 + P_1; \rho uv]^{(k)})/\partial x$ and $\mathbf{G}_y^{(k)} = \partial([\rho v, \rho uv, \rho v^2 + P_1]^{(k)})/\partial y$ indicate the gradients of flow vectors in the x and y dimension respectively; $\mathbf{S}^{(k)} = [0, S_1^{(k)}, S_2^{(k)}]$, where the second and third components indicate the crowd forces along the x and y directions, respectively; $P_1^{(k)} = h(\rho^{(k)})$ is the traffic pressure, which is assumed to result in the psychological consciousness of pedestrians attempting to maintain distance from others in the same group; and $\bar{m}$ indicates the average mass of a single pedestrian, which is assumed to be a constant in this study.

Assumption 2. *The responses of pedestrians to variations in the density of a given group are characterized as follows: in low- and high-density groups, pedestrians respond*

promptly and slowly, respectively, and pedestrians is unable to respond in extremely high-density groups.

The traffic pressure within the higher-order continuum framework represents a pseudo-pressure that characterizes the pedestrian response to variations in the density of the k-th pedestrian group, pedestrian group, as illustrated in Equation (3). Both the one-dimensional (1D) model and the two-dimensional (2D) higher-order continuum model account for hyperbolicity and isotropy. However, in the latter model, route choices are made simultaneously (Jiang et al. 2010). Consequently, this study re-evaluates the traffic pressure assumption from the perspective of the 1D anticipation characteristics of the pedestrian group, which is further discussed in the following.

$$\partial_t \mathbf{V}^{(k)} + (\mathbf{V}^{(k)} \cdot \nabla)\mathbf{V}^{(k)} + \frac{h'(\rho^{(k)})}{\rho^{(k)}} \nabla \rho^{(k)} = \text{RHS}. \tag{3}$$

The irrationality of traffic pressure, intended to maintain hyperbolicity, has been criticized in the "brake or accelerate" case since it was introduced in the Payne–Witham (PW) model (Aw and Rascle 2000). In densely crowded situations, the effective propagation of information cannot be guaranteed due to the unpredictable behavior of pedestrians, such as irregular movement (Helbing et al. 2007) and panic behavior (Helbing and Mukerji 2012). To address this problem, the proposed model considers three types of pressure–density relationships in the context of anticipation characteristics:

- In a low-density group ($\rho^{(k)} \leq \rho_0$), the movement state in the k-th pedestrian group ($V_1^{(k)}$ in Figure 3a)) is influenced by the density in neighboring regions. In particular, pedestrians try to lower their speed to avoid dense crowds nearby, even when $V_2^{(k)}$ is large. Therefore, the traffic pressure strictly increases with the density, as in many PW-type models.
- In a high-density group ($\rho^{(k)} > \rho_1$), pedestrians ($V_3^{(k)}$ in Figure 3a)) experience compression, and their behavior is highly unstable when brake or acceleration is uncertain and independent of $V_4^{(k)}$ (Loveparade 2011; Johansson et al. 2008). Moreover, the presence of a dense crowd narrows the perceptions of pedestrians, and information cannot be efficiently propagated (Figure 3b)), leading to nonpositive $h'(\rho^{(k)})$.
- In a medium-density group ($\rho_0 < \rho^{(k)} \leq \rho_1$)he movement characteristics are determined through in-between physiological anticipation. Thus, the value of the anticipation term $h'(\rho^{(k)})$ is smaller than that in the low-density situation.

This phase transition in crowd dynamics yields a segmented relationship between the density and sonic speed c, as in Equation (4), that can be applied in the 2D isotropic continuum model.

$$\sqrt{h'(\rho^{(k)})} := c = \begin{cases} c_0, & \rho^{(k)} \leq \rho_0 \\ c_0/2, & \rho_0 < \rho^{(k)} \leq \rho_1 \\ 0, & \rho^{(k)} > \rho_1 \end{cases} \tag{4}$$

Remark 1. The characteristic speeds of the PDE system can significantly differ from the sonic speed mentioned earlier, as they are also influenced by the right-hand sides in the complex system.

Assumption 3. *Panic sentiment influences not only the pushing behavior but also*

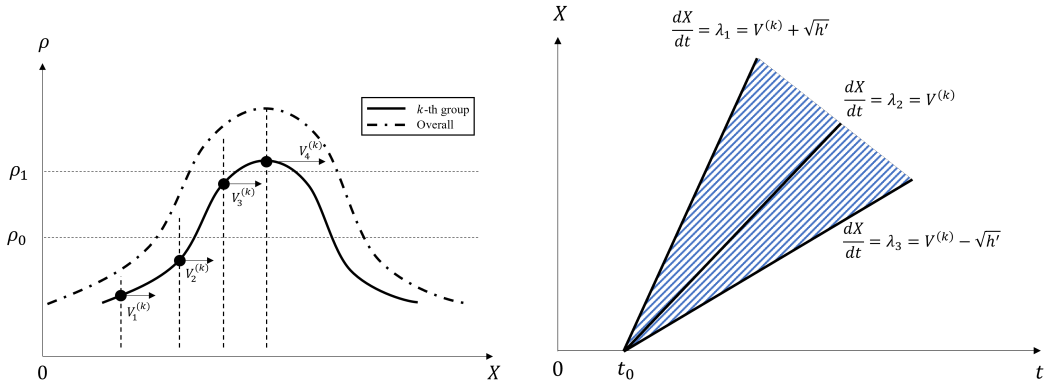

(a) problem of "brake or accelerate" (b) propagation of information

Figure 3.: **Information propagation in the k-th pedestrian stream.** (a) Example 1D case: Four pedestrians with velocity $V_i^{(k)}(i = 1, 2, 3, 4)$ are assumed with three "brake or accelerate" preferences based on the local density. (b) The characteristic speeds determined from the left-hand-side of Equation (3) generate three characteristic lines that determine the propagation area of the local density information over space and time.

the walking pattern on the fundamental diagram (FD). In general, more panic-stricken pedestrians walk faster and push harder.

The influence of panic sentiment on pushing behavior has been observed in many crowd disasters (Helbing et al. 2005; Haghani et al. 2019). In the unidirectional model proposed by Liang et al. (2021), panic sentiment is assumed to influence only the pushing behavior. However, pedestrians in high-density crowds typically wish to walk over two times faster than that in the normal condition because of the panic sentiment (Helbing et al. 2000), generating a second peak on the flow–density curve (Helbing et al. 2007). Denote the overall density as $\rho = \sum_k \rho^{(k)}$, the following speed–density relationship is applied based on the FD form proposed by Wong et al. (2010) for normal multidirectional pedestrian flow.

$$f^{(k)}(\mathbf{Q}) = v_f^{(k)} \exp(-\gamma_1^{(k)} \rho^2) \times \prod_{i=1}^{n} \exp[\gamma_2^{(k)}(1 - \cos\varphi_{ik})(\rho^{(i)})^2] \tag{5}$$

with $\gamma_1^{(k)}(\delta) = \gamma_c^{(k)}(1 - \delta^{(k)}) + \gamma_p^{(k)}\delta^{(k)}$, where $\gamma_c^{(k)}$ and $\gamma_p^{(k)}$ are the first parameters in the FD for calm and mass panic situations, respectively; $\gamma_2^{(k)}$ is the second parameter in the FD; $\delta^{(k)} \in [0, 1]$ describes the panic sentiment; and φ_{ik} denotes the intersecting angle of the expected movement directions of the i-th and k-th pedestrian stream, which is determined by the instantaneous speed distribution of the two pedestrian groups: $(\mathbf{Q}^{(i)}, \mathbf{Q}^{(k)}) \mapsto \varphi(\mathbf{Q}^{(i)}, \mathbf{Q}^{(k)})$.

The parameters for calm situations have typically been calibrated through on-site experiments (Wong et al. 2010), and only limited experimental studies have been conducted on the heterogeneity and panic influence. Therefore, in this study, empirical values are used for real crowd disasters. The simulation results are noted to be quantitatively consistent and can provide guidance for future experimental studies.

Assumption 4. *The pushing force generated in the collision area is homogeneous, and a penalty is introduced to account for the collisions of different pedestrian streams.*

Pushing force is generated only after the critical density is reached, which allows for physical contact. In this scenario, the mean walking speed gradually decreases as the standard deviation increases in the unidirectional and bidirectional flows (Lee and Lam 2006). The pushing direction may be highly unstable owing to the surrounding effects, such as the physical interactions. Therefore, the pushing force in a unit area is considered to be balanced by the different pedestrian streams, and its direction is the same as the joint speed direction. Thus, the pressure model (Liang et al. 2021) in the unidirectional case can be applied to the more general multidimensional case through the following Eikonal equation:

$$\left\|\nabla\left(\frac{P_2}{\alpha}\right)\right\| = \frac{\max\limits_k(\delta^{(k)})\cdot p(\rho)}{\alpha}\cdot\frac{\|\sum_k \rho^{(k)}\boldsymbol{\nu}_e^{(k)}\|}{\rho};\quad P_2=0\quad\text{if}\quad\alpha=0 \tag{6}$$

where α is the relaxation factor, defined in Equation (7), $p(\rho)$ indicates the relationship between the pushing capacity and density; and $\delta^{(k)}(x,y,t)\in[0,1]$ describes the panic sentiment.

$$\alpha=\begin{cases}1, & \nabla\rho\cdot(\sum_k \rho^{(k)}\boldsymbol{\nu}_e^{(k)})\geq 0\\ \max(\frac{\rho-\rho_0}{\rho_m-\rho_0},0), & \nabla\rho\cdot(\sum_k \rho^{(k)}\boldsymbol{\nu}_e^{(k)})<0\end{cases} \tag{7}$$

3.2. *Model formulation*

The mixed-type continuum model is formulated as a set of partial differential equations (PDEs) with appropriate initial and boundary conditions. Because the model corresponds to a multidirectional flow system, the PDE set for each pedestrian stream includes the conservation laws of mass and momentum; expected speed with pressure potential; and inflow boundary $\Gamma_O^{(k)}$, outflow boundary $\Gamma_D^{(k)}$ and common solid boundary Γ_H conditions.

3.2.1. Mass and momentum conservation

Equation (8) presents the conservation laws of mass and momentum for the k-th pedestrian group.

$$\mathbf{Q}_t^{(k)}+\mathbf{F}_x^{(k)}+\mathbf{G}_y^{(k)}=\mathbf{S}^{(k)}/\bar{m};\quad(\mathbf{F}^{(k)},\mathbf{G}^{(k)})=(\mathbf{F}_O^{(k)},\mathbf{G}_O^{(k)})\quad\text{if}\quad(x,y)\in\Gamma_O^{(k)} \tag{8}$$

where

$$\mathbf{Q}^{(k)} := \begin{bmatrix} q_1 \\ q_2 \\ q_3 \end{bmatrix}^{(k)} = \begin{bmatrix} \rho \\ \rho u \\ \rho v \end{bmatrix}^{(k)}, \mathbf{S}^{(k)} := \begin{bmatrix} 0 \\ S_1 \\ S_2 \end{bmatrix}^{(k)} = \begin{bmatrix} 0 \\ \bar{m}\frac{f(\mathbf{Q})q_1\nu_x - q_2}{\tau} \\ \bar{m}\frac{f(\mathbf{Q})q_1\nu_y - q_3}{\tau} \end{bmatrix}^{(k)} - \begin{bmatrix} 0 \\ \frac{\rho^{(k)}}{\rho}\frac{\partial P_2}{\partial x} \\ \frac{\rho^{(k)}}{\rho}\frac{\partial P_2}{\partial y} \end{bmatrix} \tag{9a}$$

$$\mathbf{F}^{(k)} = \begin{bmatrix} q_2 \\ \frac{q_2^2}{q_1} + h(q_1) \\ \frac{q_2 q_3}{q_1} \end{bmatrix}^{(k)} = \begin{bmatrix} \rho u \\ \rho u^2 + P_1 \\ \rho uv \end{bmatrix}^{(k)}, \mathbf{G}^{(k)} = \begin{bmatrix} q_3 \\ \frac{q_2 q_3}{q_1} \\ \frac{q_2}{q_1} + h(q_1) \end{bmatrix}^{(k)} = \begin{bmatrix} \rho v \\ \rho uv \\ \rho v^2 + P_1 \end{bmatrix}^{(k)} \tag{9b}$$

, $h(\rho^{(k)}) = \int_0^{\rho^{(k)}} c^2\, dx$ and $(\nu_x, \nu_y)^{(k)} = (u_e, v_e)^{(k)}/\|(u_e, v_e)^{(k)}\|$.

3.2.2. Equilibrium speed considering pressure potential

Two static Eikonal equations are introduced to take into account the route strategy and aggregated pushing potential.

First, this predictive user-equilibrium model is applied to determine the expected movement direction $\boldsymbol{\nu}_e^{(k)} = (\nu_x, \nu_y)^{(k)}$, as indicated in Equation (10).

$$\|\nabla \phi_e^{(k)}\| = g(\rho) + 1/f^{(k)}(\mathbf{Q}); \quad \phi_e^{(k)} = 0 \quad \text{if} \quad (x, y) \in \Gamma_D^{(k)} \tag{10a}$$

$$\boldsymbol{\nu}_e^{(k)} = -\nabla \phi_e^{(k)}/\|\nabla \phi_e^{(k)}\| \tag{10b}$$

where $g(\rho)$ indicates the local discomfort cost associated with high density.

Second, the crowd pressure for the overall pedestrian flow is determined through Equation (11).

$$\left\| \nabla \left(\frac{P_2}{\alpha} \right) \right\| = \frac{\max_k(\delta^{(k)}) \cdot p(\rho)}{\alpha} \cdot \frac{\| \sum_k \rho^{(k)} \boldsymbol{\nu}_e^{(k)} \|}{\rho}; \quad P_2 = 0 \quad \text{if} \quad \alpha = 0 \tag{11}$$

where α is the relaxation factor, defined in Equation (7), $p(\rho)$ indicates the relationship between pushing capacity and density, and $\delta^{(k)} \in [0, 1]$ describes the panic sentiment.

3.3. *Analytical properties*

This section demonstrates the mixed-type analytical property that consists of both hyperbolicity and non-hyperbolicity. Based on these analytical properties, the ability of the model to simulate the instability/turbulence phenomena observed in crowd disasters is demonstrated. Moreover, the analytical property is consistent with that in the unidirectional case if the multidirectional system is homogeneous.

Proposition 1. The Euler equation set for the k-th pedestrian group is strictly hyperbolic if $\rho^{(k)} \leq \rho_1$ but non-hyperbolic (parabolic or elliptic) if $\rho^{(k)} > \rho_1$.

According to the model formulation, the characteristics of flux vectors in each pedestrian group depend on only the crowd states of the individual group. Thus, the hyperbolicity is independent. For the k-th pedestrian group, the Jacobians of $\mathbf{F}^{(k)}$ and

$\mathbf{G}^{(k)}$ are

$$\mathbf{J}_{\mathbf{F}}^{(k)}(\mathbf{Q}^{(k)}) = \begin{bmatrix} 0 & 1 & 0 \\ -u^2 + h'(\rho^{(k)}) & 2u & 0 \\ -uv & v & u \end{bmatrix}^{(k)}, \quad \mathbf{J}_{\mathbf{G}}^{(k)}(\mathbf{Q}^{(k)}) = \begin{bmatrix} 0 & 0 & 1 \\ -uv & v & u \\ -v^2 + h'(\rho^{(k)}) & 0 & 2v \end{bmatrix}^{(k)} \tag{12}$$

For any real linear combination $\alpha_l \mathbf{J}_{\mathbf{F}}^{(k)} + \beta_l \mathbf{J}_{\mathbf{G}}^{(k)}$, the three eigenvalues are

$$\lambda_1 = \alpha_l u^{(k)} + \beta_l v^{(k)}, \qquad \lambda_{2,3} = \alpha_l u^{(k)} + \beta_l v^{(k)} \pm \sqrt{(\alpha_l^2 + \beta_l^2) h'(\rho^{(k)})} \tag{13}$$

As defined by the segment function in Equation (4), the PDE system retains its hyperbolic nature under low-density conditions ($\rho^{(k)} \leq \rho_1$). This is evidenced by the Jacobians possessing real and distinct eigenvalues when $h'(\rho^{(k)}) > 0$. However, under high-density conditions ($\rho^{(k)} > \rho_1$), the model displays either complex or identical eigenvalues within the Jacobians, a state referred to as non-hyperbolicity (a detailed introduction of hyperbolicity can be found in (Gustafsson et al. 2013)).

Proposition 2. Linear stability is maintained if (1) $\rho^{(k)} \leq \rho_1$ and (2) sonic speed c is adequately large.

First, the continuum theory in Equation (8) for each pedestrian stream ($k = 1, 2, 3 \ldots, K$) is rewritten as the following set of Euler equations:

$$\begin{cases} \rho_t^{(k)} + \nabla \cdot (\rho^k \mathbf{V}^{(k)}) = 0 \\ \mathbf{V}_t^{(k)} + \left(\mathbf{V}^{(k)} \cdot \nabla\right) \mathbf{V}^{(k)} + c^2 \frac{\nabla \rho^{(k)}}{\rho^{(k)}} = \frac{\mathbf{V}_{ep}^{(k)} - \mathbf{V}^{(k)}}{\tau^{(k)}} \end{cases} \tag{14}$$

where $\mathbf{V}_{ep}^{(k)} = \mathbf{V}_e^{(k)} - \frac{\tau^{(k)}}{\bar{m}} \cdot \frac{\nabla P_2}{\rho}$ is the equilibrium speed defined with consideration of the pressure effect.

Small perturbations of density and speed are added to the steady state $(\rho_0^{(k)}, \mathbf{V}_0^{(k)})$ of k-th pedestrian stream, which are considered to be exponential and are expressed as in Equation (15).

$$\begin{cases} \rho^{(k)} = [\rho_0 + \tilde{\rho} e^{is \cdot x + \omega t}]^{(k)} \\ \mathbf{V}^{(k)} = [\mathbf{V}_0 + \tilde{\mathbf{V}} e^{is \cdot x + \omega t}]^{(k)} \end{cases} \tag{15}$$

By substituting the permutations into Equation (14) and ignoring the nonlinear terms, the following linear equation set (16) can be obtained.

$$\mathbf{A}^{(k)} \begin{bmatrix} \tilde{\rho} \\ \tilde{u} \\ \tilde{v} \end{bmatrix}^{(k)} = 0 \tag{16}$$

where

$$\mathbf{A}^{(k)} = \begin{bmatrix} \omega + i(s_1u_0 + s_2v_0) & i\rho_0 s_1 & i\rho_0 s_2 \\ \frac{c^2 i s_1}{\rho_0} - \frac{1}{\tau}\frac{\delta(u_{ep})}{\delta\rho} & \omega + \frac{1}{\tau} + i(s_1u_0 + s_2v_0) & 0 \\ \frac{c^2 i s_2}{\rho_0} - \frac{1}{\tau}\frac{\delta(v_{ep})}{\delta\rho} & 0 & \omega + \frac{1}{\tau} + i(s_1u_0 + s_2v_0) \end{bmatrix}^{(k)} \tag{17}$$

To maintain stability, the real parts of ω derived from $\det(\mathbf{A}^{(k)}) = 0$ must be nonpositive, and thus:

$$\left[c^2(s_1^2 + s_2^2) - \left(\rho_0 \left(s_1 \frac{\delta\left(u_{ep}\right)}{\delta\rho} + s_2 \frac{\delta\left(v_{ep}\right)}{\delta\rho} \right) \right)^2 \right]^{(k)} \geq 0 \tag{18}$$

Remark 2. If $c \leq 0$, linear stability is no longer maintained in the given pedestrian stream.

If $c > 0$, $\left(s_1\frac{\delta(u_{ep})}{\delta\rho} + s_2\frac{\delta\left(v_{ep}\right)}{\delta\rho}\right)^2 \leq (s_1^2 + s_2^2)(\frac{\delta(u_{ep})}{\delta\rho})^2 + (\frac{\delta(u_{ep})}{\delta\rho})^2)$. Thus, the linear stability of the pedestrian stream holds only if c satisfies the following condition:

$$\left\| \rho_0^{(k)} \frac{\delta\left(\mathbf{V}_{ep}^{(k)}\right)}{\delta\rho^{(k)}} \right\| \leq c \tag{19}$$

Remark 3. The linear stability of the multidirectional problem holds only if all groups of pedestrians ($k = 1, 2, 3 \ldots, K$) satisfy Equation (19).

Proposition 3. If the pedestrian streams are homogeneous with identical boundary conditions, the dynamics of multidirectional systems $\mathbf{Q}_t^{(k)}$ equal those in an integrated unidirectional system $(\sum_k \mathbf{Q})_t$.

In this analysis, the dynamics at the initial time point are proven to be identical, and the following dynamics are analogous. Owing to the homogeneity of pedestrian streams, identical equilibrium walking speeds are derived using Equation (20) by substituting identical parameters and $\varphi_{ik} = 0$ in Equation(5).

$$\|\mathbf{V}_e\| = \|\mathbf{V}_e^{(k)}\| = v_f \exp(-\gamma_1\rho^2) \tag{20}$$

Correspondingly, the cost potential derived from Equation (10) and pressure potential derived from Equation (11) are identical for all pedestrian streams. Therefore, the Euler equation sets in Equation (14) are identical to

$$\begin{cases} \rho_t^{(k)} + \nabla \cdot (\rho^k \mathbf{V}^{(k)}) = 0 \\ \mathbf{V}_t^{(k)} + \left(\mathbf{V}^{(k)} \cdot \nabla\right)\mathbf{V}^{(k)} + c^2\frac{\nabla\rho^{(k)}}{\rho^{(k)}} = \frac{\mathbf{V}_{ep} - \mathbf{V}^{(k)}}{\tau} \end{cases} \quad , \quad k = 1, 2, ..., K \tag{21}$$

Given that c is constant or linearly dependent on $\rho^{(k)}$, multiply the Euler momentum equation in each equation set by $\rho^{(k)}$ and integrate the two Euler equations. The

following Euler equation set can be derived:

$$\begin{cases} (\rho)_t + \nabla \cdot \mathbf{Q}_v = 0 \\ (\mathbf{Q}_v)_t + (\mathbf{Q}_v \cdot \nabla)\, \mathbf{Q}_v + c^2 \nabla \rho = \frac{\mathbf{V}_{ep}\rho - \mathbf{Q}_v}{\tau} \end{cases} \tag{22}$$

where $\rho = \sum_k \rho^{(k)}$ and $\mathbf{Q}_v = \sum_k (\rho^{(k)} \mathbf{V}^{(k)})$. Equation (22) is equivalent to the dynamics of $(\sum_k \mathbf{Q})_t$ under the same initial values and boundary conditions.

Remark 4. The homogeneous multidirectional systems and unidirectional system are consistent only if the sonic speed c is constant or linearly dependent on $\rho^{(k)}$.

4. Mixed-type finite difference method (FDM)

Because of the existence of non-hyperbolicity, traditional numerical methods cannot be applied to the PDE sets presented in Section 2.2. To numerically solve the problem, a mixed-type FDM and the second-order total variation diminishing (TVD) Runge–Kutta scheme are developed to solve the conservation equations. The Eikonal equations are solved using the Godunov fast sweeping method (FSM).

First, Equation (8) is discretized as in Equation (23). The second-order TVD Runge–Kutta scheme, described in Algorithm 1, is introduced for time integration. At each time step, the crowd states including all pedestrian stream $\mathbf{Q}_n$ values are updated with $\mathbf{Q}_{n+1}$ until the simulation is terminated at a predefined time.

$$\begin{aligned} \mathbf{L}^{(k)}(\mathbf{Q}, t) = \frac{d\mathbf{Q}}{dt} &= -(\mathbf{F}_x^{(k)} + \mathbf{G}_y^{(k)}) + \mathbf{S}^{(k)}/\bar{m} \\ &\sim -\frac{1}{h}(\hat{\mathbf{F}}^{(k)}_{i+\frac{1}{2},j} - \hat{\mathbf{F}}^{(k)}_{i-\frac{1}{2},j}) - \frac{1}{h}(\hat{\mathbf{G}}^{(k)}_{i,j+\frac{1}{2}} - \hat{\mathbf{G}}^{(k)}_{i,j-\frac{1}{2}})) + \frac{\mathbf{S}^{(k)}(\mathbf{Q})}{\bar{m}} \end{aligned} \tag{23}$$

Two terms on the right-hand side of Equation (23), remain to be calculated: the differences between the numerical fluxes and the source term.

The Godunov FSM is introduced to numerically solve the Eikonal equations, i.e., Equations (10) and (11). The route strategy equation, Equation (10) is a standard Eikonal equation that can be directly calculated through Algorithm 2. The aggregated pressure equation, Equation (11) consists of two Eikonal equations corresponding to different regions according to the movement characteristics (Liang et al. 2021), as in Equation (24). The solution of the Eikonal equation set is not unique. Therefore, the FSM is applied to seek an approximation of the continuous solution of P_2, which is the physically relevant solution. In this condition, the Gauss–Seidel iterations in Algorithm 2 can be applied simultaneously to the two Eikonal equations, as P_2 is continuous when sweeping from one region to another.

$$\|\nabla P_2\| = \max_k(\delta^{(k)}) \cdot p(\rho) \frac{\|\sum_k \rho^k \boldsymbol{\nu}_e^k\|}{\rho}, \qquad \text{if} \quad \nabla\rho \cdot \left(\sum_k \rho^k \boldsymbol{\nu}_e^k\right) \geq 0 \tag{24a}$$

$$\|\nabla\left(\frac{P_2}{\alpha}\right)\| = \frac{\max_k(\delta^{(k)}) \cdot p(\rho)}{\alpha} \frac{\|\sum_k \rho^k \boldsymbol{\nu}_e^k\|}{\rho}, \qquad \text{if} \quad \nabla\rho \cdot \left(\sum_k \rho^k \boldsymbol{\nu}_e^k\right) < 0 \tag{24b}$$

Algorithm 1 Second-order TVD Runge–Kutta scheme

$n \leftarrow 0; \mathbf{Q}_0^{(k)} \leftarrow \mathbf{0}$ ▷ Initially, the simulation area is empty
$t_0 \leftarrow 0; \Delta t_0 \leftarrow 0.01$
while $n = 0; t_n \leq t_{max}; n++$ **do**
  while $k = 1; k \leq N; k++$ **do**
    $\tilde{\mathbf{Q}}^{(k)} \leftarrow \Delta t_n \times \mathbf{L}^{(k)}(\mathbf{Q}_n, t_n)$
  end while
  while $k = 1; k \leq N; k++$ **do**
    $\mathbf{Q}_{n+1}^{(k)} \leftarrow (\mathbf{Q}_n^{(k)})/2 + (\tilde{\mathbf{Q}}^{(k)} + \Delta t_n \times \mathbf{L}^{(k)}(\tilde{\mathbf{Q}}, t_n + \Delta t_n))/2$
  end while
  $\Delta t_n \leftarrow \mathbf{CFL}(h/\eta)$ ▷ Requirement of the CFL condition
  $t_{n+1} \leftarrow t_n + \Delta t_n$
end while

Algorithm 2 Godunov Fast Sweeping Method

$\phi_{(n_x \times n_y)} \leftarrow 10^{12}$ ▷ Initially, the potential is at maximum
while $\mathrm{NIT} = 0; \mathrm{NORM}(\phi^{new} - \phi^{old}) \leq 10^{-9}; \mathrm{NIT}++$ **do**
  while (i, j) in the GS sequences **do**
    $\mathrm{T}_x \leftarrow \min(\phi_{i-1,j}, \phi_{i+1,j})$
    $\mathrm{T}_y \leftarrow \min(\phi_{i,j-1}, \phi_{i,j+1})$
    if $|\mathrm{T}_x - \mathrm{T}_y| \geq C_{(i,j)} \times h$ **then**
      $\phi_{(i,j)}^{new} \leftarrow \min(\mathrm{T}_x, \mathrm{T}_y) + C_{(i,j)} \times h$
    else
      $\phi_{i,j}^{new} \leftarrow (\mathrm{T}_x + \mathrm{T}_y + \sqrt{2C_{i,j}^2 h^2 - (\mathrm{T}_x - \mathrm{T}_y)^2})/2$
    end if
    $\phi_{i,j}^{new} \leftarrow 0$ if $(x_i, y_j) \in \Gamma_D$ ▷ Fixed boundary condition during iterations
  end while
end while
calculate $\nabla\phi(x, y)$ by the central difference method

The mixed-type FDM (Algorithm 3), which considers the phase transition between hyperbolicity and ellipticity, is used for the approximation of the numerical fluxes. In the hyperbolic region, the eigenvalues of the Jacobi matrix are real and unique (Jacobians of $\mathbf{F}^{(k)}$ over $\mathbf{Q}^{(k)}$ are presented as an example in Equation(25)). The numerical fluxes are approximated through the traditional local Lax–Friedrichs (LF) scheme on the characteristic space.

$$\mathbf{J}_{\mathbf{F}}^{(k)}(\mathbf{Q}^{(k)}) = \begin{bmatrix} 0 & 1 & 0 \\ -u^2 + h & 2u & 0 \\ -uv & v & u \end{bmatrix}^{(k)} \tag{25}$$

and the three distinct eigenvalues are $u^{(k)}, u^{(k)} \pm c^{(k)}$.

In the non-hyperbolic region, the Jacobi matrix becomes singular, and the traditional LF splitting is not applicable. A new splitting scheme based on (Shu 1992) is introduced to capture instability in this multidimensional problem. First, we assume the following

LF splitting scheme along the x-dimension:

$$\mathbf{H}^{\pm}(\mathbf{Q}^{(k)}) = \frac{1}{2}(\mathbf{F}^{(k)}(\mathbf{Q}^{(k)}) \pm \mathbf{\Lambda}\mathbf{Q}^{(k)}), \quad \mathbf{\Lambda} = \begin{bmatrix} \lambda_1 & & \\ & \lambda_2 & \\ & & \lambda_3 \end{bmatrix} \tag{26}$$

where $\mathbf{\Lambda}$ is the eigenmatrix to be determined. The Jacobian of $\mathbf{H}^{+}$ is

$$\mathbf{J}_{\mathbf{H}^{+}}(\mathbf{Q}^{(k)}) = \begin{bmatrix} \lambda_1 & 1 & 0 \\ -u^2 + h & 2u + \lambda_2 & 0 \\ -uv & v & u + \lambda_3 \end{bmatrix}^{(k)} \tag{27}$$

and the three eigenvalues are $u + \lambda_3, u + (\lambda_1 + \lambda_2)/2 \pm \sqrt{(\lambda_1 - \lambda_2)^2 + 4u(\lambda_1 - \lambda_2) + 4h'}/2$.

Representing $M = \lambda_1 - \lambda_2$, the existence and distinctness of the three eigenvalues are ensured if

$$M = \begin{cases} 0 & \text{if} \quad h' > 0 \\ \max\limits_{\Omega,x} \left(-2 \left(|u| - \sqrt{u^2 - h'} \right) \right) + \varepsilon & \text{if} \quad h' \leq 0 \end{cases} \tag{28}$$

and

$$\lambda_2 = \max_{\Omega,x} \left(|u| + \frac{\sqrt{M^2 + 4uM + 4p'} - M}{2}, 0 \right), \tag{29}$$

where ε is a positive value and Ω is the non-hyperbolic region in the computational domain. In this model, $h' = 0$ in the non-hyperbolic region. Therefore, the eigenvalues can be expressed as

$$\begin{aligned} &\lambda_1 = \lambda_0 + \varepsilon, \\ &\lambda_2, \lambda_3 = \lambda_0 = \max_{\Omega,x} \left(|u| + \frac{\sqrt{\varepsilon^2 + 4u\varepsilon} - \varepsilon}{2}, 0 \right) \end{aligned} \tag{30}$$

where ε takes the value 0.1 in this study. Using the three eigenvalues, the LF splitting scheme can be processed along the x direction. The process along the y direction is analogous.

Algorithm 3 Mixed-type Finite Difference Method

while $i = -\frac{1}{2}; i \leq (n_x + \frac{1}{2}); i++$ **do**
  while $j = 1; j \leq n_y; j++$ **do**
    if $\rho^{(k)}_{i+\frac{1}{2},j} \leq \rho_1$ **then** ▷ Hyperbolic region
      Decompose the characteristics of Jacobi matrix $\mathbf{J_F(Q)} = \mathbf{R\Lambda R^{-1}}$
      $\mathbf{T}^{(\mathbf{Q})}_{s,j} \leftarrow \mathbf{R}(\mathbf{Q}^{(k)}_{i+\frac{1}{2},j})\mathbf{Q}^{(k)}_{s,j}; \mathbf{T}^{(\mathbf{F})}_{s,j} \leftarrow \mathbf{R}(\mathbf{Q}^{(k)}_{i+\frac{1}{2},j})\mathbf{F}^{(k)}_{s,j}$ ▷ Characteristic projection
      $\lambda^{k,H}_{i+\frac{1}{2},j} \leftarrow \max_s(\max(\mathbf{\Lambda}(\mathbf{Q}^{(k)}_{s,j})))$
      $\hat{\mathbf{T}}_{i+\frac{1}{2},j} \leftarrow \frac{1}{2}(\mathbf{T}^{(\mathbf{F})}_{i,j} + \mathbf{T}^{(\mathbf{F})}_{i+1,j} - \alpha^{k,H}_{i+\frac{1}{2},j}(\mathbf{T}^{(\mathbf{Q})}_{i,j} - \mathbf{T}^{(\mathbf{Q})}_{i+1,j}))$ ▷ LLF Scheme
      $\hat{\mathbf{F}}^{(k)}_{i+\frac{1}{2},j} \leftarrow \mathbf{R}(\mathbf{Q}^{(k)}_{i+\frac{1}{2},j})\hat{\mathbf{T}}_{i+\frac{1}{2},j}$
    else ▷ Non-hyperbolic region
      $\mathbf{\Lambda}^{k,E} \leftarrow [\lambda_0 + M, \lambda_0, \lambda_0]^T$
      $\hat{\mathbf{F}}^{(k)}_{i+\frac{1}{2},j} \leftarrow \frac{1}{2}(\mathbf{F}_{i,j} + \mathbf{F}_{i+1,j} - \mathbf{\Lambda}^{k,E}(\mathbf{Q}_{i,j} - \mathbf{Q}_{i+1,j}))$ ▷ LF for non-hyperbolic
    end if
  end while
end while
calculate the numerical fluxes $\hat{\mathbf{G}}^{(k)}_{i,j+\frac{1}{2}}$ along the y direction
$\frac{1}{h}(\hat{\mathbf{F}}^{(k)}_{i+\frac{1}{2},j} - \hat{\mathbf{F}}^{(k)}_{i-\frac{1}{2},j}) + \frac{1}{h}(\hat{\mathbf{G}}^{(k)}_{i,j+\frac{1}{2}} - \hat{\mathbf{G}}^{(k)}_{i,j-\frac{1}{2}}) \sim \nabla \cdot (\mathbf{F}^{(k)}, \mathbf{G}^{(k)})$

calculate cost potential $\nabla\phi^{(k)}(x, y)$ and pressure $\nabla P_2(x, y)$ through Algorithm 2
$\mathbf{S}^{(k)} \leftarrow \mathbf{S}_1(\nabla\phi^{(k)}(x, y)) + \mathbf{S}_2(\nabla P_2(x, y))$
$\mathbf{L}^{(k)}(\mathbf{Q}, t) \leftarrow (\mathbf{S}^{(k)}/\bar{m} - \nabla \cdot (\mathbf{F}^{(k)}, \mathbf{G}^{(k)}))$

5. Case studies

This study demonstrates the applicability of the proposed model in reflecting crowd pressure and turbulence by simulating two major crowd disasters. The first disaster simulated was the 2015 Hajj crowd disaster, which took place during a religious event in Mecca, Saudi Arabia on September 25, 2015 (BBC 2015). The second simulated disaster was the 2010 Love Parade crowd disaster, which occurred during a widely attended music festival in Duisburg, Germany on July 24, 2010 (Loveparade2010doc 2010). The video recordings from the Love Parade were assessed using the PIV method, and the processed results were compared quantitatively with the simulated data. Table 1 provides a summary of the general parameters and functions utilized in both simulations, which were determined based on empirical values.

Table 1: Parameters and functions used in the case study.

Symbol/Function	**Value**	**Meaning**
c_0	0.6 m/s	Sonic speed
$\bar{m}$	65 kg	Average weight
ρ_0	6 ped/m^2	Critical density for physical contact
ρ_1	7 ped/m^2	Critical density for phase transition
ρ_m	10 ped/m^2	Maximum density
v_f	1.034 m/s	Free flow speed
γ_c	-0.08	First parameter in the FD in calm situations
γ_p	-0.06	First parameter in the FD in panic situations
γ_2	-0.019	Second parameter in the FD
$g(\rho)$	$0.02\rho^2$	Function of the discomfort cost
$p(\rho)$	$300\sqrt{\max(0, \rho - \rho_0)}$	Function of the pushing capacity

5.1. *2015 Hajj crowd disaster*

The tragic crowd disaster during the Hajj pilgrimage in 2015 occurred during a religious procession, resulting in over 700 fatalities and 900 injuries. Based on information from post-disaster analyses (BBC 2015), this study conducted a simulation of the collision between two large groups of pedestrians heading to the same destination from the horizontal and vertical passages, representing Street 223 and Street 204, respectively, as illustrated in Figure 4. The numerical simulation was performed over a 70×50 m^2 (mesh size: 140×100) T-shaped area. As the destination for the two groups is the same, only one pedestrian stream was considered, with panic sentiment defined as in Equation (31).

$$\delta^{(1)}(x, y, t) = \begin{cases} 0 & t \leq 360\text{s} \\ (t - 360)/360 & 360\text{s} < t \leq 720\text{s} \\ 1 & 720\text{s} < t \leq 800\text{s} \end{cases}, \tag{31}$$

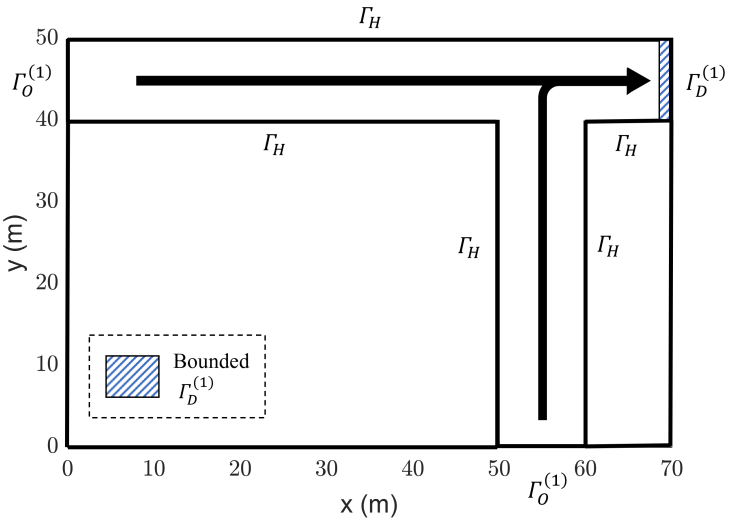

Figure 4.: **Simulation geometry of the 2015 Hajj crowd disaster.** The pedestrian stream in the simulation geometry origins from two different streets but heads to the same destination. At $t = 120$ s, the boundary $\Gamma_D^{(1)}$ was restricted because of overcrowding at the hoerizontal passage (Benedictus 2015).

The evolution of density distributions is presented in Figure C1 (Appedix C). The proposed model successfully reproduced dangerous crowd states with values comparable to those observed in crowd disasters (Fruin 1993): The maximum density was 13.87 ped/m^2, and crowd pressure was approximately 1254 N/m. The critical crowd characteristics simulated are discussed below.

5.1.1. Crowd pressure

The simulation results of the crowd pressure P_2 reveal the dangerous state of crowds in panic situations. In the time period $t \in [720, 800]$ s, pedestrians were densely packed at the intersection, allowing pushing forces to propagate through force chains. At $t = 800$ s, the maximum aggregated pressure reached 1254 N/m (refer to Figure 5a)), coinciding with an extremely high density exceeding 10 ped/m^2. Figure 5b) presents the simulated correlation between crowd pressure and density, which aligns with empirical observations (Bradley 1993): Even at high densities (approximately 7 ped/m^2), the maximum pressure in the region can increase. According to Smith and Lim (1995), an average pressure of $1,000$ N/m sustained for 30 s can cause significant discomfort and even suffocation in a densely packed crowd. The model proposed in this study successfully replicates such pressure levels during this hazardous event.

5.1.2. Crowd turbulence

The critical site during the Hajj crowd disaster was the intersection of Street 223 and Street 204 (BBC 2015), which represent the horizontal and vertical passages, respectively, as shown in Figure 4. The simulation results replicated the crowd turbulence at this highly dangerous location, as illustrated in Figure 6. In areas where the density exceeded 7 ped/m^2, the results indicated a phase transition from laminar to turbulent flow. Vortices were visible at the collision zone between the northward and eastward pedestrian streams, signifying significant turbulence and discomfort in this region.

Figure 7 depicts the flow-density relation ascertained using the calculation method

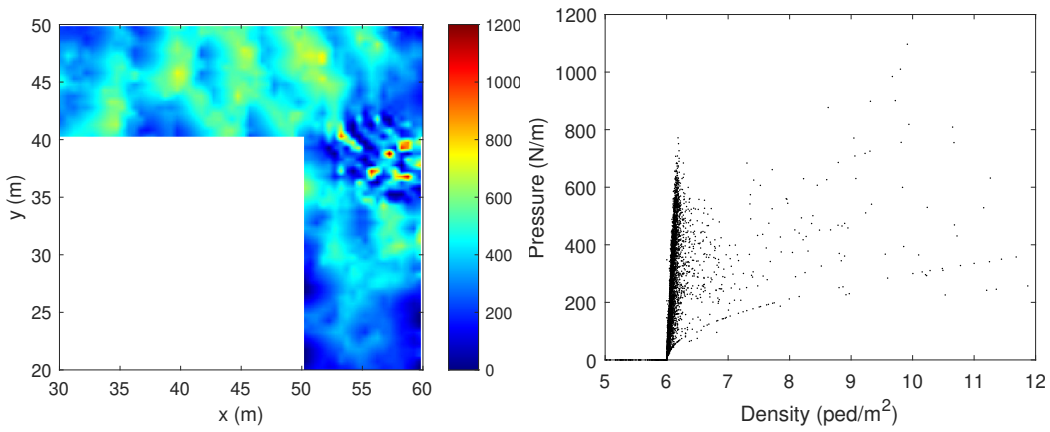

(a) pressure heatmap at $t = 800$ s (b) pressure–density relationship

Figure 5.: **Estimation of aggregated pushing pressure P_2 near the intersection.** (a) Pressure distribution around the pole. (b) The pressure–density scatter shows that the pressure has no functional relationship with the density.

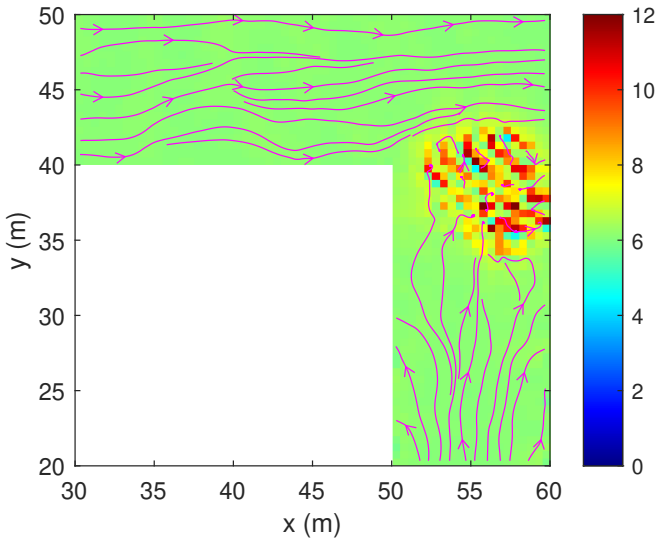

Figure 6.: **Plot of the fluid streamlines superimposed on the density heatmap at $t = 800$ s.** Vortices can be observed within the regions of extremely high density near the intersection.

presented by Liang et al. (2021). Under low-density conditions, i.e. $\rho^{(1)} \leq 6$ ped/m^2, the flow-density exhibited a "Λ"-shape but was lower than the FDs assumed in Equation (5), due to the presence of non-equilibrium states. In medium-density conditions, where $6 < \rho^{(1)} \leq 7$ ped/m^2, the system transitioned into instability, and the flow magnitude formed a "second peak" in the flow-density relation. This phenomenon has also been observed in previous empirical studies (Helbing et al. 2007). Under high-density conditions, the flow magnitude surged dramatically, indicating severe oscillations within the crowd, which could potentially lead to significant discomfort and falls. This high level of instability was also thought to influence movement in medium-density situations, as the flow rapidly increased from $\rho^{(1)} = 6.3$ ped/m^2.

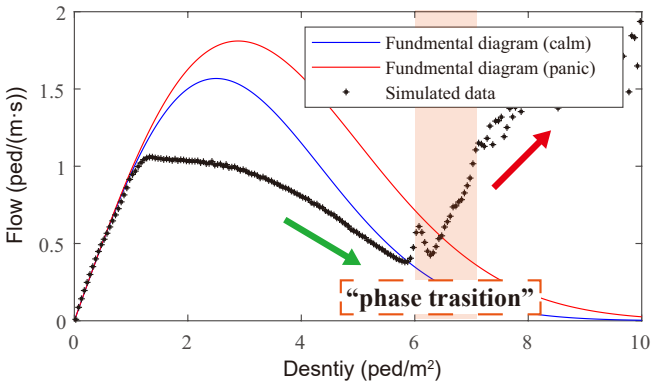

Figure 7.: **Phase transition depicted via the flow-density relation.** Although the fundamental diagrams used in the case study appear smooth, a marked phase transition is noticeable between $\rho^{(1)} \in [6, 7]$ ped/m^2. This suggests a transition in the crowd's state, moving from a stable to a turbulent condition.

5.2. *2010 Love Parade crowd disaster*

Love Parade was a popular annual dance music festival that had been held in Germany since 1989. On July 24, 2010, a severe crowd disaster occurred during this event in Duisburg, causing 21 fatalities and 652 injuries. A simulation was performed in this study to reproduce the high crowd pressure and turbulence during this disaster consistent with the empirical observations (Loveparade2010doc 2010; Helbing and Mukerji 2012). Based on known data from empirical studies and video data, the numerical simulation was performed over a 105×50 m^2 T-shaped area, involving six pedestrian streams and various boundary conditions specified in Figure 8. The panic sentiment was defined as in Equation (32) for the 5th and 6th pedestrian streams, the members of which attempted to exit the site from climbing up the pole and container, respectively (see Figure 8).

$$\delta^{(5,6)}(x, y, t) = \begin{cases} 0 & t \leq 720 \\ (t - 720)/180 & 720 < t \leq 900 \\ 1 & t > 900 \end{cases}, \tag{32}$$

The evolution of density distributions is presented in Figure C2 (Appendix C). The maximum density reproduced in this case was 12.45 ped/m^2, and crowd pressure was approximately 972 N/m. The high crowd pressure occurred with turbulence in the high-density region around the pole, where people attempted to leave the area. The crucial crowd characteristics during crowd disasters are discussed in the following.

5.2.1. Crowd pressure

The simulation results of the crowd pressure P_2 illustrate the dangerous crowd states in panic situations. In the period $t \in [900, 1200]$ s, the pedestrians were densely packed, allowing pushing forces to propagate through force chains. At $t = 1200$ s, the maximum aggregated pressure was 972 N/m (Figure 9a)), and was accompanied by an extremely high density (over 10 ped/m^2) close to the pole. Figure 9b) displays a non-functional relationship between crowd pressure and density. The proposed model successfully replicates such pressure levels, which were the direct cause of fatalities in the 2010

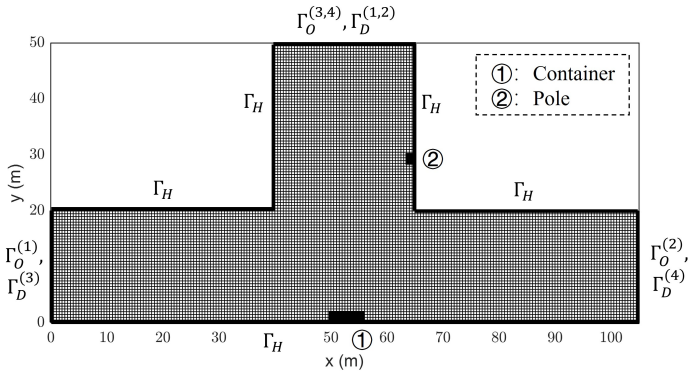

(a) $t = 0$ s

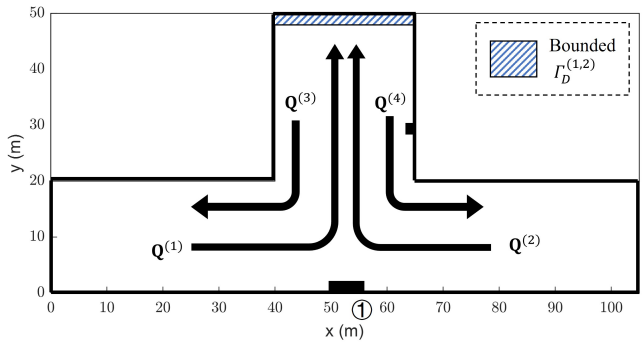

(b) $t = 300$ s

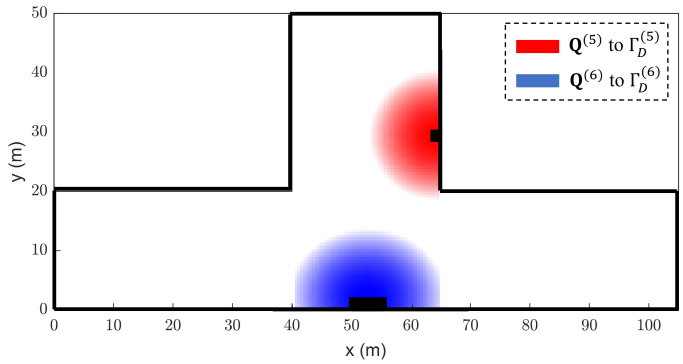

(c) $t = 720$ s

Figure 8.: **Model of the crowd disaster during the 2010 Love Parade.** (a) At $t = 0$ s, the simulation geometry (mesh size: 210×100) contains four pedestrian streams. (b) At $t = 300$ s, the boundary $\Gamma_D^{(1,2)}$ was restricted because of overcrowding at the main ramp (Loveparade2010doc 2010). (c) At $t = 720$ s, two new pedestrian streams were generated: the stranded pedestrians in the blue and red regions, who attempted to leave from the container and pole, respectively.

Love Parade crowd disaster.

5.2.2. Crowd turbulence

While turbulence did not result in any pedestrians falling during the Love Parade disaster, chaotic movement patterns were observed around the pole in both the video

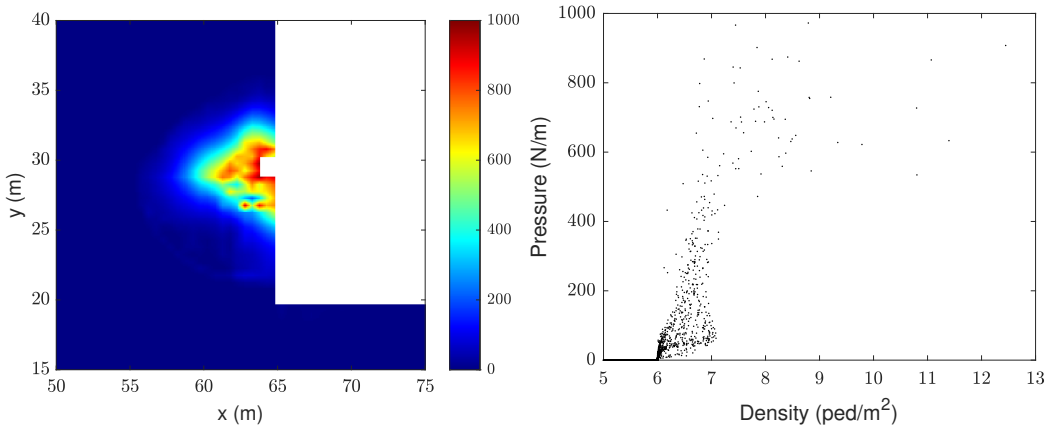

(a) pressure heatmap at $t = 1200$ s (b) pressure–density relationship

Figure 9.: **Estimation of aggregated pushing pressure P_2 at the intersection.** (a) Pressure distribution around the pole. (b) The pressure–density scatter shows that the pressure has no functional relationship with the density.

recordings (Loveparade 2011) and the simulation results (Figure 10). The VE (Appendix A) derived from the simulation results was compared with that extracted from the video to demonstrate the capability of the model in simulating crowd turbulence. The PIV method (Appendix B) was used to quantify the crowd turbulence through video recordings.

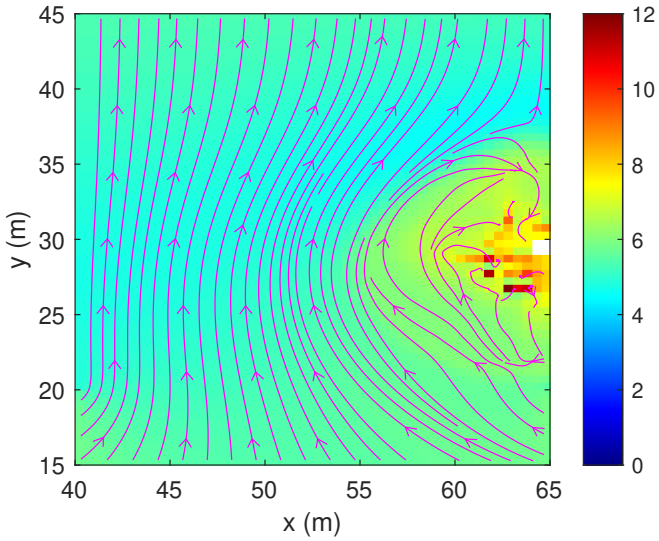

Figure 10.: **Plot of the fluid streamlines superimposed on the density heatmap at $t = 1200$ s.** Vortices can be observed within the regions of extremely high density surrounding the pole.

As shown in Figure 11, the VE varied from 1.23 to 3.93 in direction entropy and from 1.74 to 3.20 in magnitude entropy between 16:38:10-16:38:20 (see Figure 2a), when turbulent waves could be identified from the video through a long-term photographic procedure (Johansson et al. 2008). During the simulation period of $t \in [750, 1000]$ s, the VE was also calculated within the same region, as detailed in Appendix B. The computed VE showed a significant increase from 2.13 ($t = 750$ s) to 4.16 ($t = 1000$ s) in

direction entropy and from 0.94 ($t = 750$ s) to 2.27 ($t = 1000$ s) in magnitude entropy. This trend indicated an increasing level of chaos in the simulated crowd movement, which mirrored the observations from the video analysis.

Moreover, despite the high density around the pole, the crowd continued to move. The average velocity of 0.0265 m/s, calculated from the simulation results in the observed area during $t \in [750, 1000]$ s, was similar to the value of 0.0192 m/s obtained by the PIV method (Figure 11c). Notably, the processed results from the video recordings were more oscillatory because the video was captured from the top and thus included head shaking, which may have increased the instability.

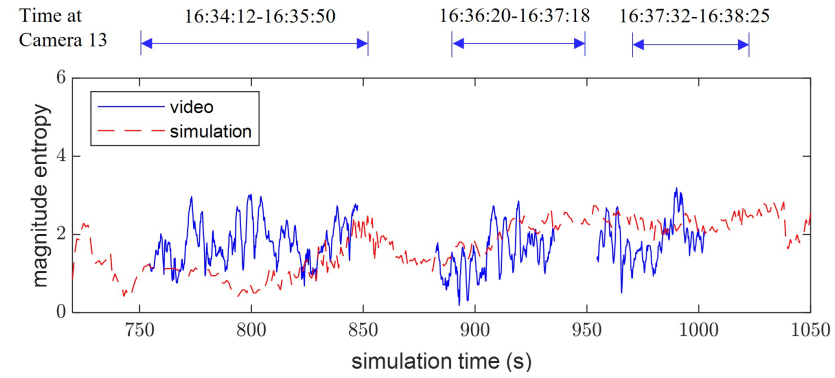

(a) evolution of magnitude entropy

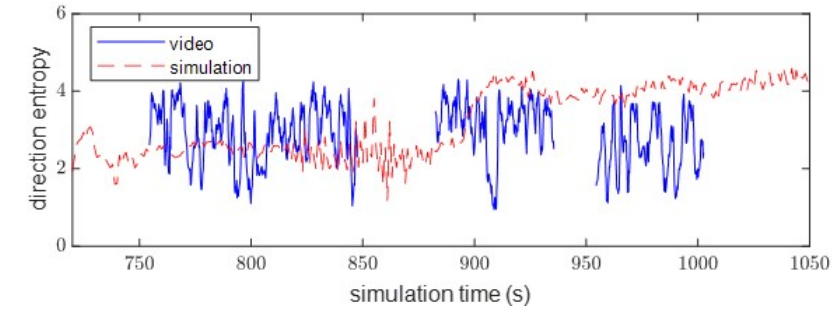

(b) evolution of direction entropy

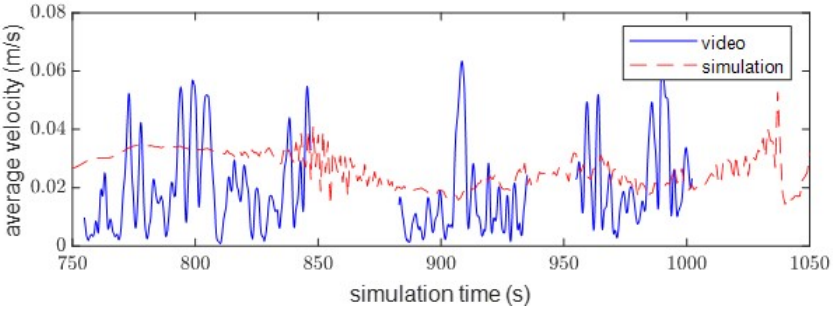

(c) evolution of average velocity

Figure 11.: **Quantification of crowd turbulence during the 2010 Love Parade.** (a,b) Comparison of the VE derived through the simulation and PIV method in the period $t \in [750, 1050]$ s, which is analogous to the situation between 16:34:12 and 16:38:42. (c) Comparison of the simulated and observed evolution of average velocity.

6. Model performance

The effectiveness of the model was demonstrated through the case studies of real-world crowd disasters. According to empirical research and data (Loveparade2010doc 2010; Helbing and Mukerji 2012; BBC 2015), the following characteristics of crowd dynamics were observed during the crowd disaster, which were required to be considered in the simulation.

Situation: The primary cause of crowd accumulation was the trapping of pedestrians in critical areas. This also led to an increase in crowd density and extended waiting times, thereby escalating the sense of panic. In the simulation of the 2015 Hajj crowd disaster, congestion at the destination on the horizontal street induced impatience among two large groups of pedestrians. Similarly, in the simulation of the 2010 Love Parade crowd disaster, desperation set in among the pedestrians who attempted to escape the area by climbing poles and containers. The design of layout settings and boundary conditions was informed by these observations.

Turbulence: The simulation results displayed notable vortexes in critical regions, aligning with empirical findings (BBC 2015; Loveparade2010doc 2010). This is particularly evident in the 2010 Love Parade crowd disaster, where pedestrians near the pole were forced to move chaotically, as captured in the video (Loveparade 2011). This precarious situation indicated an increasing variation in pressure within the dense crowd, which was replicated in the simulations as crowd turbulence.

Pressure: The first death during the 2010 Love Parade crowd disaster occurred near the pole and was reported to be caused by suffocation (Loveparade2010doc 2010). In the simulation, the crowd pressure P_2 increased to nearly $1,000$ N/m near the pole. A similar level of crowd pressure was replicated in the simulation of the 2015 Hajj crowd disaster. While limited research has been conducted to determine the precise pressure in such crowds, these findings align with empirical values that could potentially lead to suffocation.

Notably, the risk-level indicators included in this study, such as crowd density, crowd pressure, and VE, are important for establishing efficient crowd management strategies. These indicators can represent the features of crowd dynamics during dangerous situations. Based on the findings of the case study, the following suggestions were identified for the police and layout designers:

Small exits should be avoided when a crowd becomes dense and panicked. Dangerous crowd dynamics, such as high pressure and turbulence, were observed around the pole, attributable to the pedestrians wishing to climb the pole. Thus, small or narrow exits, such as at the pole, must be avoided, and the police must prohibit people from climbing. In the actual situation, the police pulled pedestrians from the pole, increasing their desperation to push and escape, thereby aggravating the situation.

By alleviating the panic sentiment, the pushing forces and thus the crowd pressure can be decreased. During the 2010 Love Parade crowd disaster, mobile phone connectivity was restricted due to overload (Helbing and Mukerji 2012), making people more impatient and panicked. To prevent similar tragedies, adequate communication services should be provided for large events with many attendees, such as by increasing the capacity of the base station or maintaining radio broadcasting services.

7. Conclusion

A mixed-type continuum model was developed for multidirectional pedestrian flow to reproduce complex crowd dynamics during crowd disasters. The proposed model can ensure stability when describing laminar multidirectional pedestrian flow and commonly observed stop-and-go waves and simulate crowd features in high-density conditions, such as extremely high crowd pressure and turbulence.

The analytical properties of the proposed model were explored to demonstrate its effectiveness in describing the phase transition of crowd dynamics in multidirectional systems. Furthermore, the consistency of the homogeneous multidirectional systems and unidirectional system was verified.

The model was utilized to simulate two real-world scenarios: the 2015 Hajj crowd disaster and the 2010 Love Parade crowd disaster. The simulation results, such as those for the crowd pressure and crowd turbulence, were consistent with the findings of empirical studies of crowd dynamics. Several recently developed risk-level indicators, such as the crowd pressure and VE, were incorporated to verify the effectiveness of the model in simulating crowd disasters.

Future research can conduct extensive experiments or site surveys to calibrate the key parameters and functions considered in the model, such as the sonic speed, pushing capacity, and multidirectional FDs in panic situations. Moreover, more advanced numerical schemes can be used to increase the simulation efficiency. To prevent crowd disasters, it is necessary to establish data-driven approaches to identify the panic sentiment in real-time. These approaches can be combined with the proposed analytical model for effective crowd detection and management.

Acknowledgements

The work described in this paper was supported by grants from the Research Grants Council of the Hong Kong Special Administrative Region, China (Project Nos. 17201318 and 17204919) and the National Natural Science Foundation of China (Project No. 52302378). The first author was supported by the Shanghai Super Postdoctoral Incentive Program. The third author was supported by National Key R&D Program of China (Grant No. 2021YFA0719200). The fourth author was supported by NSF grant DMS-2010107. The last author was supported by the Francis S Y Bong Professorship in Engineering from the University of Hong Kong.

References

Aw, A. A. T. M. and Rascle, M. (2000). Resurrection of 'second order' models of traffic flow. *SIAM Journal on Applied Mathematics*, 60(3):916–938.

BBC (2015). Hajj stampede: at least 717 killed in saudi arabia.

Benedictus, L. (2015). Hajj crush: how crowd disasters happen, and how they can be avoided.

Bradley, G. E. (1993). A proposed mathematical model for computer prediction of crowd movements and their associated risks. In *Proceedings of the International Conference on Engineering for Crowd Safety*, pages 303–311. Elsevier Publishing Company London.

Dickie, J. F. and Wanless, G. K. (1993). Spectator terrace barriers. *Structural Engineer*, 71:216–222.

F., A. (2022). Seoul crowd crush: what we know so far about halloween deaths in itaewon.

Fruin, J. (1993). *The causes and prevention of crowd disasters*, pages 99–108. Elsevier, Amsterdam, Netherlands.

Gustafsson, B., Kreiss, H., and Oliger, J. (2013). *Time dependent problems and difference methods*, volume 2. Wiley Online Library.

Haghani, M., Cristiani, E., Bode, N., Boltes, M., and Corbetta, A. (2019). Panic, irrationality, and herding: Three ambiguous terms in crowd dynamics research. *Journal of Advanced Transportation*, 2019:9267643.

Helbing, D., Buzna, L., Johansson, A., and Werner, T. (2005). Self-organized pedestrian crowd dynamics: Experiments, simulations, and design solutions. *Transportation Science*, 39(1):1–24.

Helbing, D., Farkas, I. J., and Vicsek, T. (2000). Simulating dynamical features of escape panic. *Nature*, 407(6803):487–490.

Helbing, D., Johansson, A., and Al-Abideen, H. Z. (2007). Dynamics of crowd disasters: An empirical study. *Physical Review E*, 75(4):046109.

Helbing, D. and Mukerji, P. (2012). Crowd disasters as systemic failures: Analysis of the love parade disaster. *EPJ Data Science*, 1(1):1–40.

Huang, L., Chen, T., Wang, Y., and Yuan, H. (2015). Congestion detection of pedestrians using the velocity entropy: A case study of love parade 2010 disaster. *Physica A: Statistical Mechanics and its Applications*, 440:200–209.

Huang, L., Wong, S. C., Zhang, M., Shu, C., and Lam, W. H. K. (2009). Revisiting hughes' dynamic continuum model for pedestrian flow and the development of an efficient solution algorithm. *Transportation Research Part B*, 43(1):127–141.

Hughes, R. L. (2002). A continuum theory for the flow of pedestrians. *Transportation Research Part B*, 36(6):507–535.

Jiang, Y. Q., Zhang, P., Wong, S. C., and Liu, R. X. (2010). A higher-order macroscopic model for pedestrian flows. *Physica A: Statistical Mechanics and its Applications*, 389(21):4623–4635.

Johansson, A., Helbing, D., Al-Abideen, H. Z., and Al-Bosta, S. (2008). From crowd dynamics to crowd safety: A video-based analysis. *Advances in Complex Systems*, 11(04):497–527.

Khan, S. D. (2019). Congestion detection in pedestrian crowds using oscillation in motion trajectories. *Engineering Applications of Artificial Intelligence*, 85:429–443.

Krausz, B. and Bauckhage, C. (2012). Loveparade 2010: Automatic video analysis of a crowd disaster. *Computer Vision Image Understanding*, 116(3):307–319.

Langston, P. A., Masling, R., and Asmar, B. N. (2006). Crowd dynamics discrete element multi-circle model. *Safety Science*, 44(5):395–417.

Lee, J. Y. S. and Lam, W. H. K. (2006). Variation of walking speeds on a unidirectional walkway and on a bidirectional stairway. *Transportation Research Record*, 1982(1):122–131.

Liang, H., Du, J., and Wong, S. C. (2021). A continuum model for pedestrian flow with explicit consideration of crowd force and panic effects. *Transportation Research Part B*, 149:100–117.

Liu, C., Song, W., Fu, L., Lian, L., and Lo, S. (2017). Experimental study on relaxation time in direction changing movement. *Physica A: Statistical Mechanics and its Applications*, 468:44–52.

Loveparade (2011). Kamera13-1620-1640.mp4.

Loveparade2010doc (2010). Dokumentation der ereignisse zur loveparade 2010 in duisburg.

Shu, C. (1992). A numerical method for systems of conservation laws of mixed type admitting hyperbolic flux splitting. *Journal of Computational Physics*, 100(2):424–429.

Smith, R. A. and Lim, L. B. (1995). Experiments to investigate the level of 'comfortable' loads for people against crush barriers. *Safety Science*, 18(4):329–335.

Still, G. K. (2022). Crowd safety and crowd risk analysis.

Thielicke, W. and Sonntag, R. (2021). Particle image velocimetry for matlab: Accuracy and enhanced algorithms in pivlab. *Journal of Open Research Software*, 9:1–14.

Wang, C., Shen, L., and Weng, W. (2023). Modelling physical contacts to evaluate the individual risk in a dense crowd. *Scientific Reports*, 13(1):3929.

Wang, J., Ni, S., Shen, S., and Li, S. (2019). Empirical study of crowd dynamic in public

gathering places during a terrorist attack event. *Physica A: Statistical Mechanics and its Applications*, 523:1–9.

Wong, S. C., Leung, W. L., Chan, S. H., Lam, W. H. K., Yung, N. H. C., Liu, C. Y., and Zhang, P. (2010). Bidirectional pedestrian stream model with oblique intersecting angle. *Journal of Transportation Engineering*, 136(3):234–242.

Yang, L., Liang, H., Du, J., and Wong, S. C. (2023). Positivity-preserving discontinuous galerkin methods on triangular meshes for macroscopic pedestrian flow models. *Journal of Advanced Transportation*, 2023:7245723.

Zhao, R., Hu, Q., Liu, Q., Li, C., Dong, D., and Ma, Y. (2019). Panic propagation dynamics of high-density crowd based on information entropy and aw-rascle model. *IEEE Transactions on Intelligent Transportation Systems*, 21:4425–4434.

Appendix A. Velocity Entropy (VE)

To quantitatively describe the risk level of the crowd state, the VE (Huang et al. 2015) is derived based on the speed distribution, which denotes the dispersion of the velocity distribution in terms of magnitude and direction. A higher VE corresponds to greater crowd instability (Wang et al. 2019). The VE has two components: magnitude entropy E_m and direction entropy E_d, defined in Equations (A1) and (A2), respectively. The velocity magnitude is divided into 10 bins of the same width (0.01 m/s) ranging from 0 to 0.1 m/s. The speed direction is divided into 36 bins of the same width (10∘) ranging from 0 to 360∘.

$$E_m = -\sum_{i=1}^{n_1} p_v(i) \log_2 p_v(i) \tag{A1}$$

where $p_v(i) = h_m(i)/N$. $h_m(i)$ indicates the number of moving particles with the velocity magnitude corresponding to the i-th bin. N indicates the total number of moving particles and n_1 is the total number of velocity magnitude bins.

$$E_d = -\sum_{j=1}^{n_2} p_\theta(j) \log_2 p_\theta(j) \tag{A2}$$

where $p_\theta(j) = h_\theta(j)/N$. $h_\theta(j)$ indicates the number of moving particles with the velocity magnitude corresponding to the j-th bin and n_2 is the total number of angle bins.

Appendix B. Particle Image Velocimetry (PIV)

The video recording of Camera 13 from 16:35 to 16:40 is processed using the PIV method (Figure B1). First, four reference points are selected according to perspective rays in a sample video frame to ensure that these rays form a rectangle after perspective transformation. The missing points during the transformation are filled by median imputation, and the size of the rectangle is estimated with consideration of the following reference objects: the width of the main ramp is approximately 25 m, and the distance between two neighboring railings is approximately 2 m. Therefore, the rectangular box (enclosed by red lines) is estimated to be a 12×12 m^2 square after perspective transformation. The observation area in this study is the 3×3 m^2 region around the

pole (blue box). After choosing the observation area, a PIV tool (Thielicke and Sonntag 2021) based on the cross-correlation algorithm is introduced to calculate the speed distribution with the time increment $\Delta t = 0.2$ s.

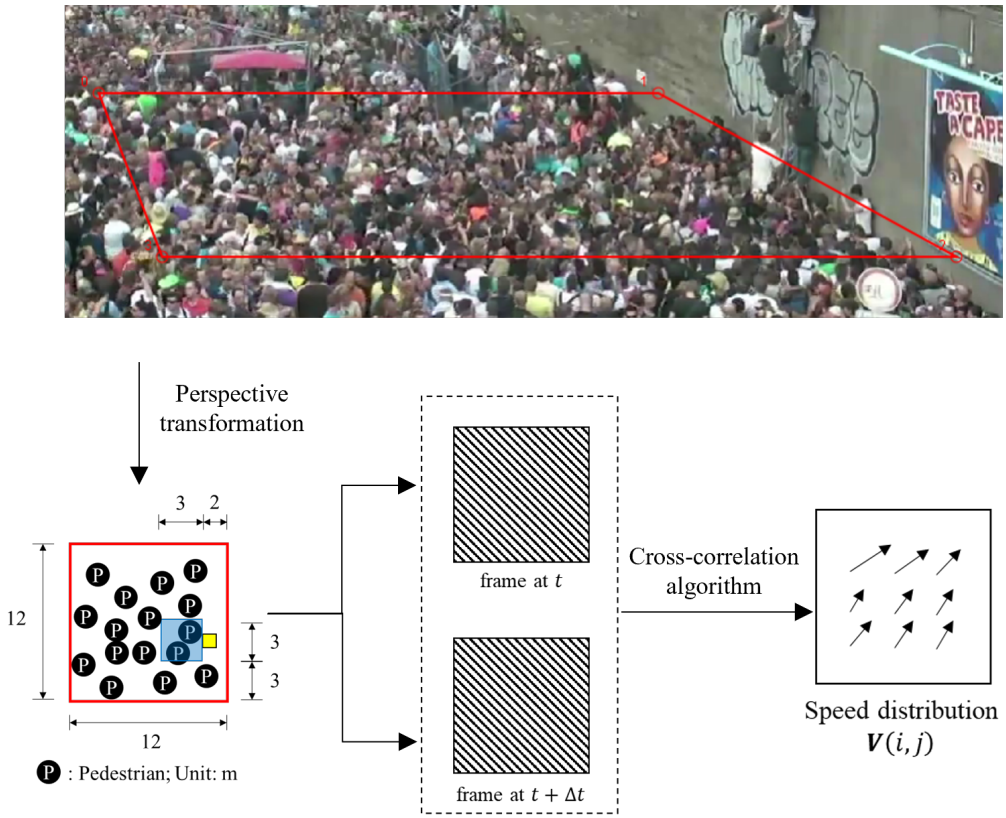

Figure B1.: **PIV processing using sample video frames.** The yellow and blue boxes indicate the pole location and observation area, respectively.

Appendix C. Evolution of Density Distributions

The evolution of density distributions in the case studies is illustrated in Figures C1 and C2. The heatmaps have lower and upper bounds of 0 and 12 ped/m^2, respectively.

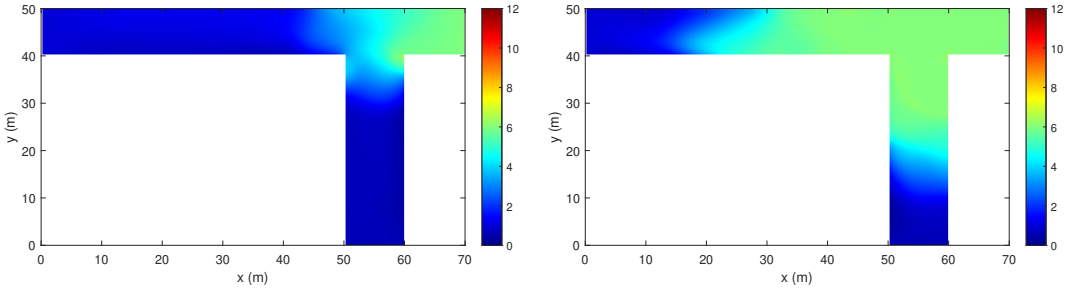

(a) $t = 200$ s (b) $t = 400$ s

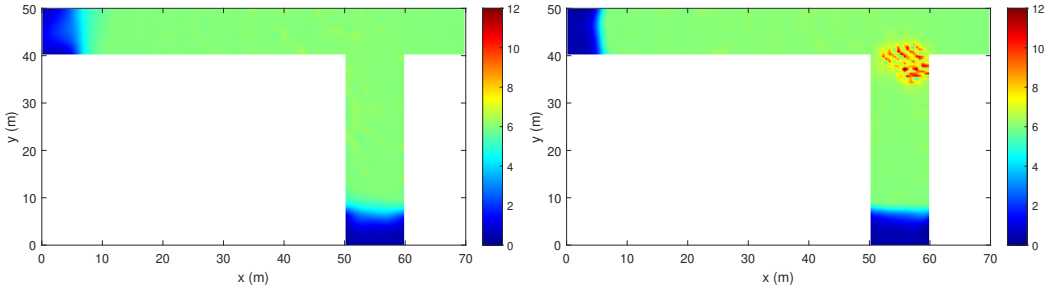

(c) $t = 600$ s (d) $t = 800$ s

Figure C1.: Simulated density evolution during 2015 Hajj crowd disaster

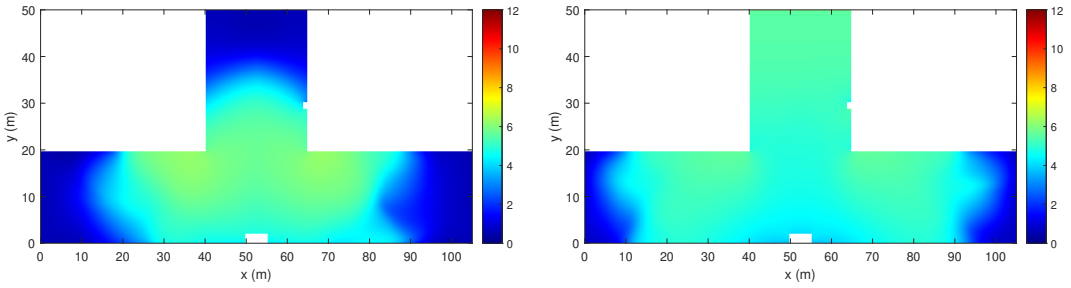

(a) $t = 300$ s (b) $t = 600$ s

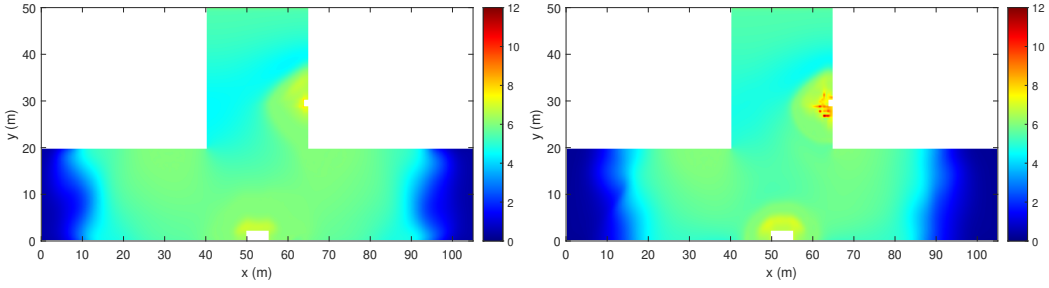

(c) $t = 900$ s (d) $t = 1200$ s

Figure C2.: Simulated density evolution during 2010 Love Parade crowd disaster

Appendix D. List of Symbols and Functions

Table D1: List of symbols and functions used in this study

Symbol/Function	**Meaning**
ρ	Overall density
$\rho^{(k)}$	Density of the k-th pedestrian group
ρ_0	Critical density for physical contact
ρ_1	Critical density for phase transition
ρ_m	Maximum density
α	Relaxation factor in the eikonal equation for crowd pressure
γ_1	First parameter in the FD
γ_c	First parameter in the FD in calm situations
γ_p	First parameter in the FD in panic situations
γ_2	Second parameter in the FD
λ_i	i-th eigenvalue
$\tau^{(k)}$	Relaxation time of the k-th pedestrian group
$\boldsymbol{\nu}_e^{(k)}$	Normalized expected speed direction of the k-th group of pedestrians
φ_{ik}	Intersecting angle between the i-th and k-th pedestrian streams
$\phi^{(k)}$	Cost potential of the k-th pedestrian group
$\delta^{(k)}$	Measurement of the panic sentiment of the k-th pedestrian group
Γ_O^k	Inflow boundary of the k-th pedestrian group
Γ_D^k	Outflow boundary of the k-th pedestrian group
Γ_H	Solid boundary
c	Sonic speed
c_0	Parameter to determine the sonic speed
E	Velocity entropy
E_d	Direction entropy of speed
E_m	Magnitude entropy of speed
$\bar{m}$	Average mass of a pedestrian
P_1	Traffic pressure
P_2	Aggregated pushing pressure
t	Time

Continued on next page

Table D1: List of symbols and functions used in this study (Continued)

$u^{(k)}$	Velocity of the k-th pedestrian group in the x direction
$u_e^{(k)}$	Expected velocity of the k-th pedestrian group in the x direction
$u_{ep}^{(k)}$	Equilibrium speed with consideration of the pressure effect of the k-th pedestrian group in the x direction
$v^{(k)}$	Velocity of the k-th pedestrian group in the y direction
$v_e^{(k)}$	Expected velocity of the k-th pedestrian group in the y direction
$v_{ep}^{(k)}$	Equilibrium speed with consideration of the pressure effect of the k-th pedestrian group in the x direction
$v_f^{(k)}$	Free-flow velocity in the FD
$\mathbf{V}^k$	Speed vector of the k-th pedestrian group
$\mathbf{V}_e^k$	Expected speed vector of the k-th pedestrian group
$\mathbf{V}_{ep}^k$	Equilibrium speed vector with consideration of the pressure effect of the k-th pedestrian group
x	Horizontal axis
y	Vertical axis
$\mathbf{X} \mapsto \mathbf{J_H}(\mathbf{X})$	Jacobian of vector $\mathbf{H}$ over vector $\mathbf{X}$
$\mathbf{X} \mapsto f^{(k)}(\mathbf{X})$	Function of FD of the k-th pedestrian group
$x \mapsto h(x)$	Function of the traffic pressure
$x \mapsto g(x)$	Function of the discomfort cost
$x \mapsto p(x)$	Function of the pushing capacity